The Astrophysical Journal, 687:997–1003, 2008 November 10

THE ROTATING NUCLEAR STAR CLUSTER IN NGC 4244

Anil C. Seth,[1,2] Robert D. Blum,[3] Nate Bastian,[4] Nelson Caldwell,[1] and Victor P. Debattista[5]

Received 2008 June 16; accepted 2008 July 15

ABSTRACT

We present observations of the nuclear star cluster in the nearby edge-on spiral galaxy NGC 4244 using the Gemini Near-Infrared Integral Field Spectrograph (NIFS) with laser guide star adaptive optics. From a previous study of edge-on galaxies, this nuclear star cluster was found to be one of a sample of clusters that appear flattened along the plane of their host galaxies disks. Such clusters show evidence for multiple morphological components, with younger/bluer disk components and older/redder spheroidal components. Our new observations of NGC 4244 show clear rotation of 30 km s^{-1} within the central 10 pc (0.5″) of the cluster. The central velocity dispersion is found to be 28 ± 2 km s^{-1}. The multiple stellar populations inferred from the optical colors and spectra are seen as variations in the CO line strength in the NIFS spectra. The rotation is clearly detected even in the older, more spheroidal stellar component. We discuss evidence for similar structures and kinematics in the nuclear star clusters of other galaxies including M33 and the Milky Way. Our observations support two possible formation mechanisms: (1) episodic accretion of gas from the disk directly onto the nuclear star cluster; or (2) episodic accretion of young star clusters formed in the central part of the galaxy due to dynamical friction.

Subject headings: galaxies: formation — galaxies: individual (NGC 4244) — galaxies: kinematics and dynamics — galaxies: nuclei — galaxies: spiral — galaxies: star clusters

Online material: color figures

1. INTRODUCTION

Prominent nuclear star clusters (NSCs) are found in ∼75% of late-type spiral galaxies (Böker et al. 2002) and early-type galaxies (Côté et al. 2006). These NSCs are intrinsically very luminous, with typical $M_I \sim -12$, and sizes similar to globular clusters ($r_{\rm eff} \sim 5$ pc; Böker et al. 2004). Recently, multiple studies (Ferrarese et al. 2006; Wehner & Harris 2006; Rossa et al. 2006) have shown that NSC masses are coupled to the mass of their host galaxy, following a similar M-σ relation as massive black holes (MBHs) and extending this relation to lower mass galaxies. This result suggests that the formation of both types of objects are linked to the formation of their host galaxies. Some galaxies host both NSCs and MBHs, but the relationship between these two types of objects is unknown (Seth et al. 2008). Unlike black holes, the assembly history of NSCs can, in principle, be inferred from studies of their stellar populations and kinematics. Thus, NSCs provide important tools for studying the history of galaxy centers and their connection to the galaxies as a whole.

In spiral galaxies, integrated optical spectra of NSCs show that they nearly always have multiple stellar populations (Walcher et al. 2006; Rossa et al. 2006). More specifically, NSCs typically have a young stellar population (<100 Myr) but are dominated in mass by stars older than >1 Gyr. Further support to this picture comes from the observations of several distinct populations in the color-magnitude diagram of the nucleus of the Sgr dwarf spheroidal (M54; Monaco et al. 2005; Siegel et al. 2007).

In Seth et al. (2006, hereafter Paper I), we found from a study of edge-on galaxies that in some NSCs these multiple stellar populations appear to be associated with different morphological components. These clusters are flattened along the major-axis of the galaxy and have color maps and morphologies that suggest they consist of young disks and older more spheroidal components.

We present here follow-up observations of the NSC in NGC 4244, the nearest galaxy in the Paper I sample ($D = 4.3$ Mpc, $1'' = 21$ pc; Seth et al. 2005). In Paper I we presented optical spectra of this cluster that indicate the presence of multiple stellar populations. Although the detailed star formation history is not well constrained, populations of 50–100 Myr combined with older populations are required to provide a good fit to the spectra. Redshifted emission identified with an H II region offset by 19 pc along the major axis of the cluster gives a lower limit to the mass of $\sim 2.5 \times 10^6\ M_\odot$. This mass measurement is consistent with the masses derived from the stellar population fitting of the spectrum as well.

In § 2 we describe the observations and data reduction. Our results on the kinematics, morphology, and stellar populations of the cluster are presented in § 3. We discuss the results in the context of other galaxies and formation models in § 4.

2. OBSERVATIONS AND DATA REDUCTION

K-band spectra of the NGC 4244 nuclear star cluster were obtained using the Near-Infrared Integral Field Spectrograph (NIFS; McGregor et al. 2003) on Gemini North, an image-slicing integral field unit spectrograph. The spectrograph was used in conjunction with the ALTAIR Laser Guide Star system. The cluster itself was used as a tip/tilt star but is too faint ($r = 16.18$) to get the highest Strehl performance. The cluster was observed in *K* band on the nights of 2007 February 9 and April 29. In total 5×900 s exposures were obtained on-source and 4×900 s exposures off-source (sky). The air mass of the observations ranged between 1.11 and 1.42, and an A0 star, HIP 50459, was observed on both nights at similar air mass to be used as a telluric calibrator. The exposures

[1] Harvard-Smithsonian Center for Astrophysics, 60 Garden Street Cambridge, MA 02138; aseth@cfa.harvard.edu.
[2] Center for Astrophysics Fellow.
[3] National Optical Astronomy Observatory, 950 North Cherry Avenue, Tucson, AZ 85721.
[4] Institute of Astronomy, University of Cambridge.
[5] Centre for Astrophysics, University of Central Lancashire, Preston PR1 2HE, UK; RCUK Fellow.

all had similar image quality, with the PSF FWHM varying by <30% between the exposures. We note that *H*-band spectral observations of the NGC 4244 NSC were obtained as well, but due to a number of observational problems and a significantly lower resolution, these data are not discussed here.

The data were reduced using the Gemini version 1.9 IRAF package, using pipelines based on the `nifsexamples` scripts. To obtain a clean telluric absorption spectra from the HIP 50459 observations, the spectra were processed as described for the science images below, after which one-dimensional spectra were extracted and the Brγ absorption line was fit and removed.

For the science exposures, an off-source exposure was subtracted from each on-source exposure; for the February 9 data only one off-source exposure was available and was thus subtracted from both images. The images were then sliced up and rectified based on Ronchi mask and arc lamp images using `nftransform` and spatially rebinned into image cubes using `nifcube`. In this process, the original $0.043'' \times 0.1''$ pixels get rebinned into $0.05''$ pixels which are block replicated in the long (slice) direction. Each data cube was then corrected for telluric absorption using the `nftelluric` program, which allows for interactive correction of the small differences in the wavelength calibration and air mass between the observations of the calibrator and each exposure. The final data cubes from each individual on-source exposure were combined using `gemcombine`, correcting for spatial and spectral offsets. The resulting data cube has a $\sim 3'' \times 3''$ field of view with $0.05''$ spatial pixels and 2.132 Å spectral pixels from 2.00–2.44 μm. Based on measurements of the sky lines, the spectral resolution is $\sim$4.1 Å (53 km s^{-1}) FWHM. The spatial resolution in the combined image was measured using four compact sources after subtracting the NSC model (§ 3.1) and found to be $0.23''$ FWHM. These four compact sources are shown as crosses in Figure 1; three of the four are also detected as pointlike sources in the higher resolution ($0.08''$ FWHM) *HST* images. The spatial resolution of our data cube is roughly $\sim$2 times lower than that achieved when using a brighter tip/tilt star (e.g., for our telluric calibrators).

A spectrum from the inner $0.1''$ of the cluster is shown in Figure 1. The plotted spectrum is the normalized flux ratio of the galaxy spectrum to the Brγ-corrected A0 V telluric calibrator spectrum. All the spectral analysis presented below is done using flux-ratioed spectra. In order to achieve a reasonable signal-to-noise ratio (S/N) for analysis of the outer parts of the cluster, the data were spatially binned using the Voronoi tesselation method described in (Cappellari & Copin 2003). The S/N of each pixel was determined empirically using a relatively featureless portion of the spectra between 22140 and 22866 Å. Individual pixels near the center of the image have S/N > 50 pixel^{-1}. We binned pixels together in order to obtain a S/N $\sim$ 25 in each bin, so near the center, the "bins" consisted of a single pixel. We found that the S/N did not increase as expected with binning (at least in part due to spectral rebinning during the initial reduction); thus, the outer bins have S/N of <10.

We also reconstructed a calibrated *K*-band image of the nuclear star cluster for the morphological analysis presented in § 3.1. To do this, we first multiplied the spectra by a 9500 K blackbody to correct for the division by the A0 telluric calibrator and then multiplied this spectrum by the 2MASS K_s filter response curve before collapsing the data cube to an image. We then calibrated the zero point of this image by comparing the flux from the best fitting model (described below) to the magnitude of the source in the 2MASS Point Source Catalog ($K_s = 13.55$; Cutri et al. 2003). Based on the variation between models and the uncertainty in the sky-level on our image, this zero point should be good to $\sim$10%.

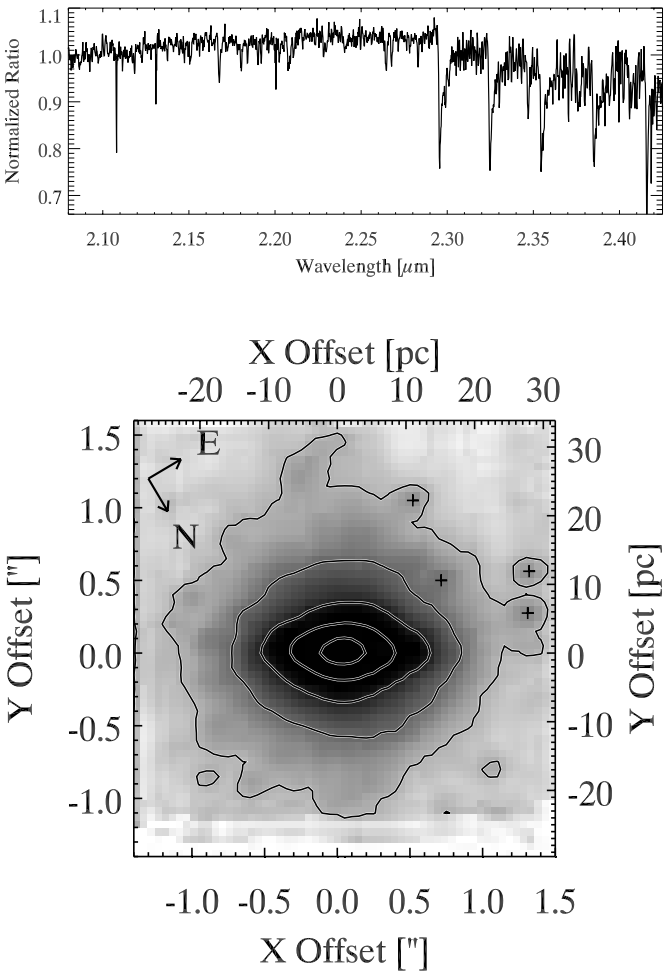

FIG. 1.—*Top*: Spectrum within $0.1''$ of the nuclear star cluster center. The plotted spectrum is the normalized flux ratio of the galaxy spectrum to the Brγ-corrected A0 V telluric calibrator spectrum. The CO band heads dominate the red part of the spectrum while Mg I (21080, 22830 Å), Brγ (21676 Å), Na I (22075 Å), and Ca I (22644–77 Å) lines are also seen. *Bottom*: *K*-band image made from collapsing the final data cube along the spectral direction. Contours are at 16.5, 15.5, 14.5, 13.5, and 12.5 mag arcsec^{-2}. Crosses show the four compact sources used to determine the spatial resolution of the data. The compass in the top left shows the rotation of the field (P.A. = 147°); the *x*-axis runs roughly along the major axis of the galaxy.

The image and calibrated contours are shown in the bottom panel of Figure 1.

3. RESULTS

In this section we present results from our Gemini NIFS *K*-band observations. We first discuss morphological fits to our high-resolution *K*-band image (§ 3.1). We then present the kinematics of the cluster in § 3.2 and its stellar populations in § 3.3. The most significant finding is that the NGC 4244 NSC is strongly rotating. Comparison of the kinematics to the stellar populations and morphological fits shows that this rotation is occurring even off the major axis of the cluster where older stellar populations appear to dominate.

3.1. *Morphological Results*

We briefly describe our analysis of the morphology of the NGC 4244 NSC using the high-resolution *K*-band image of the cluster created from our Gemini NIFS data. This information is used in § 3.3 to argue that the entire cluster is rotating and will be used as input for dynamical modeling (F. de Lorenzi et al.

TABLE 1
Results of Morphological Fits

Parameter	Values			
	NSC Disk Component Fits			
	μ_0 ($L_\odot$ pc^{-2})	h_x (pc)	z_0 (pc)	
K-band **disk**+Sérsic.....	1.4×10^5	3.39	1.19	
K-band **disk**+King	1.9×10^5	2.72	1.38	
F814W **disk**+King.....	9.7×10^4	2.73	1.42	
	NSC Spheroidal Component Fits			
	μ_0 ($L_\odot$ pc^{-2})	$r_{\rm eff}$ (pc)	(b/a)	
K-band disk+**King**	4.5×10^4	13.6	0.79	
F814W disk+**King**.....	5.3×10^4	5.70	0.73	
	$\mu_{\rm eff}$ ($L_\odot$ pc^{-2})	$r_{\rm eff}$ (pc)	(b/a)	n
K-band disk+**Sérsic**	8.7×10^3	10.9	0.81	1.68

Note.—All quantities derived assuming a distance of 4.3 Mpc.

2008, in preparation) using NMAGIC code (de Lorenzi et al. 2007).

As we found for the optical data (see Paper I, Fig. 4), a single-component elliptical King (or Sérsic) profile fit to the *K*-band image leaves behind significant residuals in the plane of the galaxy. Combined with the optical color difference (Fig. 3, *top*), this motivates us to fit the data using both a spheroidal *and* disk component. All models were convolved by a Gaussian PSF with FWHM of 0.23″ during the fitting process. We tried both disk+King (as used in Paper I) and a disk+Sérsic profile. Both profiles provide fits with reduced χ^2 values ~4 times smaller than the spheroidal component alone. The values of the derived parameters for these fits and the disk+King F814W filter fit from Paper I are shown in Table 1. The parameters for the disk fits are the central surface brightness μ_0, the scale length h_x, and scale height z_0. For the spheroidal component fits, the parameters are the central surface brightness μ_0 (King) or effective surface brightness $\mu_{\rm eff}$ (Sérsic), effective radius $r_{\rm eff}$, axial ratio (b/a), and Sérsic index n. The derived *K*-band disk sizes are very similar to those derived at optical wavelengths from the *HST* data despite the lower resolution of these data. The spheroid geometry is significantly more extended in the *K*-band, but its size is quite sensitive to the fitted value of the background.

Based on disk fits to the full galaxy from 2MASS presented in Seth et al. (2005) the central luminosity surface density of the NSC is ~250 times greater than that of the disk, while the luminosity surface density at the edge of the NIFS field is comparable to the level predicted by the galaxy disk model. Deprojecting the disk components, the luminosity volume density at the center of the NSC is $\sim 10^6$ times that of the underlying galaxy disk. The local volume density of the cluster thus dominates the mass in the central regions of the galaxy out to the edge of our data.

3.2. *Kinematic Results*

We first describe the two ingredients used to derive the kinematics of the NGC 4244 nuclear star cluster: (1) spectral templates and (2) a method to determine the line-of-sight velocity distribution (LOSVD) from the binned spectra based on the templates.

Spectral templates were obtained from two sources. Three template stars were observed with NIFS by Davidge et al. (2008) in a configuration identical to ours. Spectra for these stars were kindly provided by the author. Their spectral types, K1 III, K5 III, and M0 III, are representative of the spectral types of the red giant branch (RGB) and asymptotic giant branch (AGB) stars most likely to dominate our spectrum. We also use a larger library of spectral templates that has been observed by C. Winge using the somewhat higher resolution (3.35 Å FWHM) GNIRS spectrograph on Gemini South.[6] This library contains stars from spectral type F7–M3 and includes dwarf, giant, and some supergiant stars.

To determine the LOSVD of each spectrum we used the penalized pixel fitting (PPXF) method of Cappellari & Emsellem (2004). The program finds the best matching set of templates and convolves them to find the best fitting LOSVD, which is parameterized using a Gauss-Hermite series. The non-Gaussian terms ($h3$ and $h4$; see van der Marel & Franx 1993) in the LOSVD are penalized; thus, the solution typically converges to a Gaussian LOSVD at low S/N. The method also compensates for any low-frequency differences between the template and galaxy spectral shape using Legendre polynomials. We fit the area of the spectrum from 22900 to 24000 Å, which is dominated by strong CO lines. We calculated errors on the LOSVD parameters using Monte Carlo tests that consisted of adding noise to the spectrum based on the measured S/N and remeasuring the LOSVD 250 times without penalizing non-Gaussian distributions. The typical standard deviation on the velocity and dispersion for pixels with S/N ~ 25 is ~3 km s^{-1}. When using GNIRS templates, we convolve the template spectra by a Gaussian with $\sigma = 13$ km s^{-1} to correct for the slightly higher resolution of the GNIRS data.

We show the radial velocity map derived using PPXF on each spectral bin in the top panel of Figure 2. We show only data with reliable measurements by clipping bins with S/N < 10 or errors on the velocity above 15 km s^{-1}. *The radial velocity map shows strong rotation in the NGC 4244 NSC*. The rotation velocities reach an amplitude of 30 km s^{-1} at ~0.4″ from the nucleus. Assuming a Keplerian disk, this rotation suggests a mass of $1.7 \times 10^6\ M_\odot$ enclosed within the central 8 pc. Beyond this radius, there is some suggestion the velocity may drop, although, due to the low S/N at large radii, this result is not robust.

Based on the morphological results presented in the previous section, the NSC dominates the mass in the center of NGC 4244, and thus is likely to be kinematically distinct from the rotation of the overall galaxy disk. Olling (1996) has presented a study of the H I rotation curve of NGC 4244 with resolution as high as 10″ × 20″. The H I gas rotates in the same direction as the NGC 4244 NSC. The innermost point in their derived rotation curve is at 24″ where the galaxy rotation is 35 km s^{-1}, increasing to 60 km s^{-1} at 47″. Given that we observe rotation of ~30 km s^{-1} within the central half-arcsecond, this suggests that the rotation of the NSC is distinct from the gas component of the galaxy disk. It would be interesting to compare the NSC rotation to the stellar rotation in the galaxy disk; however, this would require relatively deep long-slit spectroscopy (e.g., Yoachim & Dalcanton 2008), since the surface brightness of the galaxy beyond the nuclear star cluster is quite low.

The line-of-sight velocity dispersion is a somewhat more difficult quantity to measure accurately due to the low dispersion of the cluster as a whole. Our spectra have 2.1 Å/28 km s^{-1} pixels and 4.1 Å/53 km s^{-1} resolution (FWHM), while the dispersions of NSCs in late-type galaxies are typically ~25 km s^{-1} (Walcher

[6] See http://www.gemini.edu/sciops/instruments/nir/spectemp/index.html.

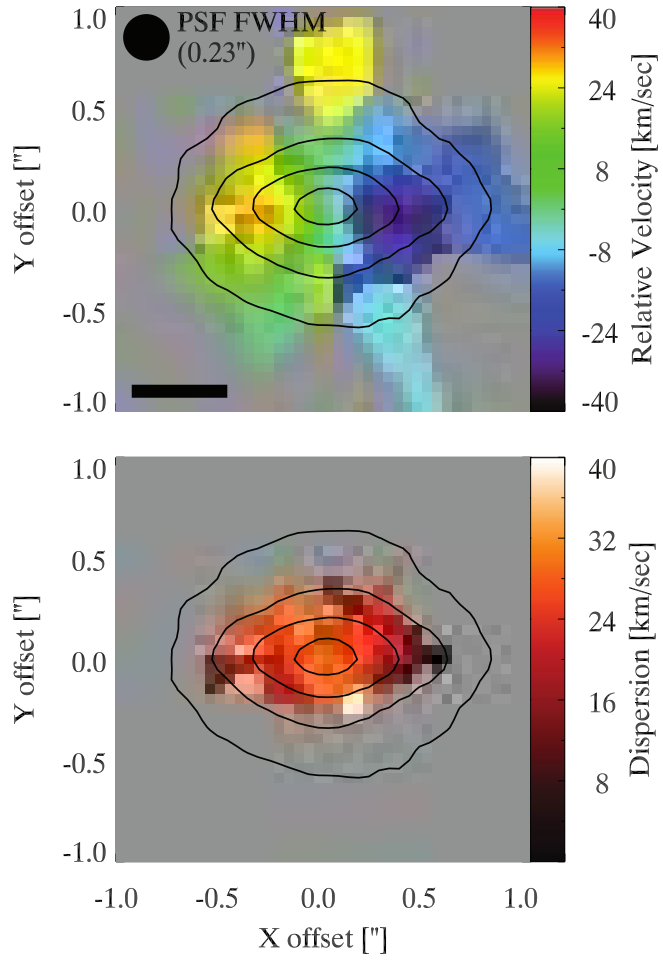

FIG. 2.—*Top*: Color indicates the measured radial velocity for the Voronoi binned data using templates observed with NIFS. Gray areas indicate spectra with S/N < 10 and/or errors >15 km s^{-1}. Rotation of ~30 km s^{-1} is clearly visible along the major axis. Contours show the *K*-band image at 15.5, 14.5, 13.5, and 12.5 mag arcsec^{-2}. The black bar indicates 10 pc (0.47″). *Bottom*: Velocity dispersion measurements with S/N > 15 and errors <10 km s^{-1}. The dispersion drops away from the center, indicating a relatively cold disk population.

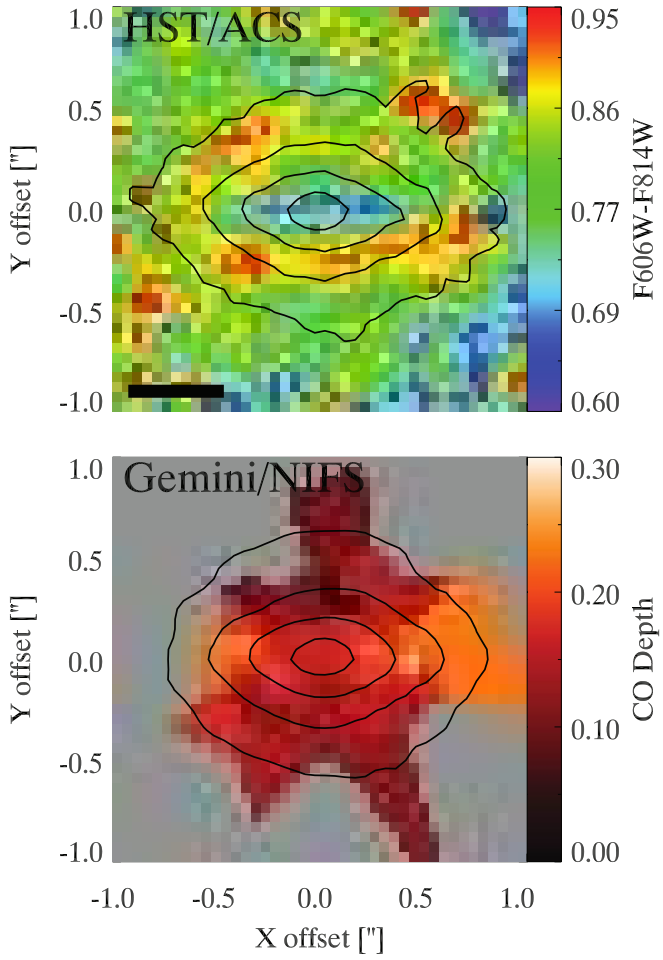

FIG. 3.—*Top*: 2″ × 2″ image of the F606W − F814W color map from the *HST* ACS data described in Paper I. The image has been rotated to match the orientation of the NIFS data. The contours indicate the F814W surface brightness and were chosen to roughly match the *K*-band contours in Fig. 2 and in the bottom panel. The black bar indicates 10 pc (0.47″). *Bottom*: 2″ × 2″ image of CO line strength, with larger values indicating deeper CO lines. The contours show *K*-band contours as in Fig. 2.

et al. 2005). Nonetheless, we are able to make an accurate measurement of the central dispersion of the cluster, $\sigma = 28 \pm 2$ km s^{-1}. Convolution of the templates with this dispersion substantially (by a factor of 2) improves the χ^2 of their fit to the central spectrum of the cluster, giving a reduced χ^2 of 0.9 and 1.1 using the GNIRS and NIFS templates, respectively. The bottom panel of Figure 2 shows a map after clipping data with S/N < 15 or errors in the dispersion >10 km s^{-1}. The velocity dispersion drops along the major axis to values of 10–20 km s^{-1} at precisely the area where rotation is seen most strongly indicating that we are indeed seeing a relatively cold rotating disk. This dispersion is close to the limit of what we can reliably recover from our relatively low resolution observations, thus these values may represent upper limits. It is unclear whether the increased dispersion we see in the center is a result of unresolved rotation or a genuinely hot component.

The use of the templates from NIFS and GNIRS give very similar results for both the velocities and dispersions. The GNIRS templates selected for fitting the spectra are primarily at spectral types close to those (K–M giants) represented by the three NIFS spectra. For almost all the spectra, our measured non-Gaussian $h3$ and $h4$ components of the LOSVD were consistent with zero. However, due to our low S/N and resolution, we would not expect to be able to detect any non-Gaussian signatures (Cappellari & Emsellem 2004).

3.3. *Stellar Populations and Connection to Kinematics*

From the optical data described in Paper I, the NGC 4244 NSC has two distinct stellar populations—a bluer population dominates in the midplane with a redder population dominating above and below the plane. This is clearly seen in the *HST*-based color map shown in the top panel of Figure 3. We would expect the NIFS data to resolve these different populations despite the 2 times lower resolution. If we make a map of the CO line strength (Fig. 3, *bottom*), the bluer areas of the *HST* image clearly have stronger CO absorption than the redder areas above the midplane. The CO line strength is determined by comparing the average depth of the line at rest wavelengths of 22957 ± 52 Å to the continuum measured just to the blue of the CO band head [^{12}CO (2, 0); Kleinmann & Hall 1986]. We also measured these values for the GNIRS template stars for comparison. The CO line strength values for the NSC range from ~0.10 above and below the major axis typical of late G-type giant stars ($T_{\rm eff} \sim 4800$ K), to ~0.25 along the major axis, typical of K3–K6 giants ($T_{\rm eff} \sim 4100$ K). We caution that the CO depth depends on the gravity of the stars as well as their effective temperature. We note that while Mg, Ca,

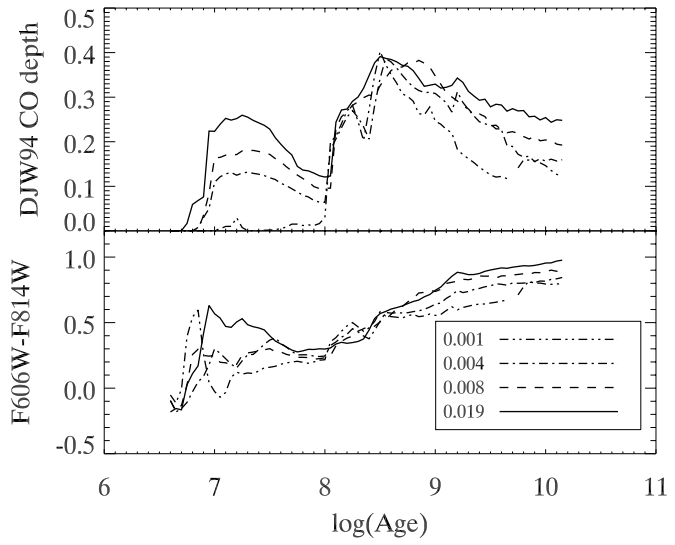

FIG. 4.—Models of the optical color CO line strength using Padova isochrones Marigo et al. (2008) at $Z = 0.004$, 0.008, and 0.019. The top panel shows the CO line strength derived using relations from Doyon et al. (1994), while the bottom panel shows the F606W − F814W optical color. [*See the electronic edition of the Journal for a color version of this figure.*]

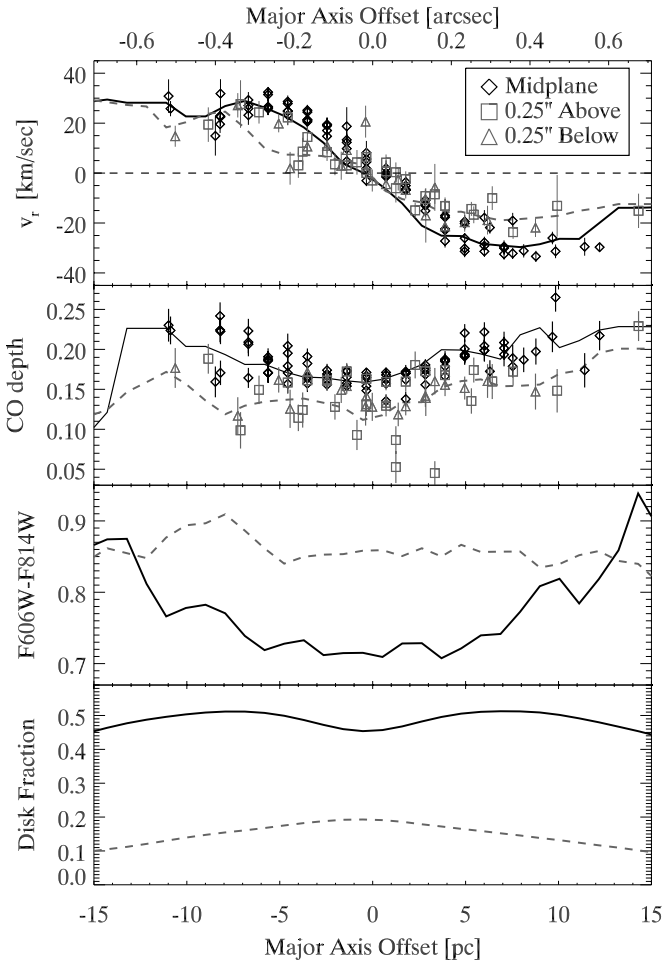

FIG. 5.—Profiles (*top to bottom*) of relative radial velocity, CO line strength, optical (F606W − F814W) color, and fraction of light expected from the disk based on the morphological models. Each quantity is plotted for the midplane (*black solid line and symbols*) and for slices above and below (*gray dashed line and symbols*) the major axis. Lines show vertically binned averages in each slice, while the symbols in the top two panels show the values of each bin that fell within our slices. [*See the electronic edition of the Journal for a color version of this figure.*]

and Brγ absorption are clearly detected in the highest S/N spectra, these features have lower S/N than the CO feature and do not show any obvious variations across the NSC. No emission features are detected.

To better understand the relation between the optical colors and CO line strengths seen within the cluster, in Figure 4 we model these quantities using Padova isochrones, which include an updated treatment of the asymptotic giant branch (AGB) (Marigo et al. 2008). We sampled 10^7 $M_\odot$ of stars from a Kroupa (2001) initial mass function and then obtained effective temperature, gravities, and the F606W, F814W, and K-band magnitudes for each star from the isochrones at ages from 4 Myr to 14 Gyr. To obtain estimates for the CO line strength, we used the relations from Doyon et al. (1994), who fit CO line strength as a function of effective temperature for dwarfs, giants, and supergiants. The total CO line strength at each age was calculated as the mean CO line strength weighted by the K-band luminosity of each star. We note that the broader Doyon et al. (1994) CO index has values that are 20%–50% lower than the one we measure here; nonetheless, the trends of CO depth with age should be robust. We also caution that the models remain very uncertain, especially given that the CO strength can be dominated by the coolest, thermally pulsing AGB stars, which are very difficult to model (Marigo et al. 2008). The CO line strength shows peaks at two ages: first at 10–20 Myr due to the presence of bright red supergiant stars, and second at ~300 Myr from AGB stars. The CO evolution of these models is qualitatively similar to that seen in the models of Maraston (2005), which also include contributions from thermally pulsing AGB stars, but differs from earlier models that do not include this phase and thus are lacking the second peak in CO depth (e.g., Leitherer et al. 1999).

We can use these models to qualitatively analyze the variations in stellar population seen across the cluster in Figures 3 and 5. The extinction is not well known; however, spectroscopic fits suggest an $A_V \sim 0.5$ corresponding to a reddening of ~0.2 mag in the F606W − F814W color. For the youngest stars, we expect a metallicity of $Z \sim 0.008$ based on the 100 km s^{-1} circular velocity of NGC 4244 (Garnett 2002). However, the combination of the red color and low CO values above and below the midplane of the cluster suggest an old (≳1 Gyr), more metal-poor population. Along the major axis there is a slight reddening in the optical color along with an increase in the CO line strength. One possible explanation for this is an age gradient within the disk; for instance if the center had an age of ~100 Myr years then the redder colors and deeper CO could result from slightly older or younger populations at 5–10 pc. We caution that the stellar populations at any point in the cluster are clearly mixed, and thus information determined from comparing the observations to single-stellar population models should be viewed with caution. With the maturing of NIR stellar models and spectral libraries (e.g., Lançon et al. 2007; Mármol-Queraltó et al. 2008), future population synthesis studies may be able to provide more robust results on the resolved star formation history from this type of data. Finally, we note that it is possible for thermal emission from warm dust to reduce the strength of the CO absorption. However, the low star formation activity in the NSC indicated by the lack of NIR emission lines suggests that dust emission probably does not play a large role in this cluster.

We now turn to the relation between the stellar populations and the rotation. Figure 5 shows the derived velocity, CO line strength, optical color, and disk fraction of the NGC 4244 NSC as function

of position in slices along, above, and below the major axis. The slices are each 0.25″ in height, and the plotted lines are the result of averaging the maps (i.e., Figs. 2 and 3) along the vertical direction in each slice at every pixel along the *x*-direction. The velocity and CO measurements were made using the Voronoi binned data; the symbols in these panels show the light-weighted positions of the bins coded by which slice they fell in.

The top panel of Figure 5 shows that the rotation is not confined to the midplane, but is present ∼0.25″ above and below the midplane as well. The bottom three panels show that the slices above and below the plane are clearly sampling a different component/stellar population from the midplane. The CO lines are less deep away from the plane, while the optical color is redder. The disk fraction in the bottom panel is based on the results of our morphological decomposition from § 3.1. We calculated the fraction of disk light along our slices from the best fitting Sérsic+disk model after convolving each component with the PSF. For the area above and below the major axis, only 10%–20% of the light in our NIFS observations appear to be coming from the disk. Taken together, *these plots show that the whole cluster is rotating, not just the bluer, younger disk component*. This finding places strong constraints on the formation of this NSC as detailed in the following section.

4. DISCUSSION AND CONCLUSIONS

In NGC 4244 we find a flattened nuclear star cluster with multiple components, a younger disk structure, and an older spheroidal structure (Paper I). From our NIFS data, we have shown that the cluster is rotating at ±30 km s^{-1} within the central 10 pc of the cluster. This rotation is not confined just to the younger disk component, but also appears to be present in the older, more spheroidal component.

There are two basic models for NSC formation: (1) globular clusters which collect at the center due to dynamical friction (Tremaine et al. 1975; Lotz et al. 2001); or (2) episodic accretion of gas onto the center followed by in situ star formation (Milosavljević 2004; Bekki 2007). A third alternative (3), combining these two scenarios, has recently been proposed by M. Milosavljevic & Agarwal (2008, private communication) in which NSCs form from young star clusters in the inner part of the galaxy disk which are massive enough to accrete onto the nucleus. These mechanisms are not exclusive: NSCs could form from a combination of these effects, and different types of galaxies may have different dominant mechanisms. However, our observations for NGC 4244 strongly conflict with the first scenario. If a significant fraction of the NSC were formed from globular clusters distributed in a spheroidal distribution, no rotation would be expected. Thus, the primary formation mechanism must be through episodic accretion of material from the disk of the galaxy, either gas or young star clusters. Distinguishing between gas and star cluster accretion may be possible through comparison of our kinematic data with simulations. Direct evidence of gas accretion into the central ∼10 pc is seen in a couple nearby nuclear star clusters using CO observations (Schinnerer et al. 2003, 2006).

There is substantial evidence that the structure we see in NGC 4244 is not unique, and in fact may be typical for NSCs in spiral galaxies. In Paper I, 5/9 NSCs in edge-on spirals were significantly flattened along the major axis of the galaxy disk, with 3 showing clear composite morphologies. NGC 4244 is the nearest of these galaxies and thus presents the clearest view of these structures. There is also evidence for similar structures in earlier type galaxies; Balcells et al. (2007) find a number of disky "nuclear extended components" with scale lengths as small as 5 pc in a sample of early-type spirals and elliptical galaxies. Previous studies of nuclei in large samples of spirals (Böker et al. 2002; Carollo et al. 2002) have focused on face-on galaxies making the structures in the disk plane difficult to detect. And very few galaxies have the parsec-scale quality of kinematic data that we have here. However, where these data exist there is evidence for nuclear structures similar to those presented here.

The Milky Way hosts a nuclear star cluster centered on Sgr A*, first noted by Becklin & Neugebauer (1968). The luminosity profile of the inner ∼100 pc of the Milky Way is distinct from the underlying bulge and disk profiles (e.g., Serabyn & Morris 1996). This component is clearly flattened along the galactic plane (axial ratio of 0.45; Catchpole et al. 1990), but less so in the central 30 pc, which led Launhardt et al. (2002) to propose the existence of two components, a $3 \times 10^7\ M_\odot$ NSC dominating the central 30 pc (with $r_{\rm eff} \sim 10$ pc) and a more massive nuclear stellar disk extending out to 100–200 pc. Numerous young OH/IR stars are found, primarily within the central 40 pc, and these have a flattened distribution with rotation of >100 km s^{-1} (Lindqvist et al. 1992). Based on integrated *K*-band spectra, McGinn et al. (1989) find that the central dispersion is ∼125 km s^{-1} and drops quickly with increasing radius, while the rotation increases outward equaling the dispersion at a radius of ∼3 pc, the edge of their study. Compared to the NGC 4244 NSC, the Milky Way appears quite similar, but scaled up by ∼10 times in mass and ∼3 times in size, rotation, and dispersion, as would be expected for a more massive galaxy. The very center (<1 pc) of the Milky Way NSC has been intensively studied and shows complex dynamics with striking differences between older stars and very young (<10 Myr) stars. The latter show ordered rotation (and counterrotation!) and provide evidence for processes 2 (Genzel et al. 2003) and 3 (e.g., Maillard et al. 2004; Lu et al. 2005) described above.

There is also evidence for flattening and rotation in the M33 NSC. This cluster is elongated along the major axis of the galaxy with an axial ratio of ∼0.85 (Lauer et al. 1998; Matthews & Wood 2001). At a radius of ∼1″ (4 pc), the rotation is ∼8 km s^{-1} and dispersion is 27 km s^{-1} (Gebhardt et al. 2001). Even considering that the orientation is likely not edge-on, it appears that the rotation does not dominate in the M33 NSC to the same extent as in NGC 4244.

In conclusion, we have shown above that the nuclear star cluster in NGC 4244 is rotating. The rotation is seen in both the young disk and older spheroid components, suggesting that accretion of gas or star clusters from the disk is the dominant mechanism in the formation of this NSC. While there is some evidence that other NSCs in spiral galaxies have similar structures (and thus formation histories), a better understanding of NSC formation across Hubble type will require a detailed study resolving the stellar populations and kinematics of numerous nearby NSCs.

The authors thank Tracy Beck, Andre Wong, and Richard McDermid for their help with the observation planning and analysis. We thank Tim Davidge for giving us his spectral templates. This paper was much improved by the suggestions of the referee, Torsten Böker. We also acknowledge helpful conversations with Thomas Puzia, Kevin Covey, Dawn Erb, and Andrés Jordán. A. S. gratefully acknowledges the support of the Center for Astrophysics Postdoctoral Fellowship. Based on observations obtained at the Gemini Observatory, which is operated by the

Association of Universities for Research in Astronomy (AURA), Inc., under a cooperative agreement with the National Science Foundation (NSF) on behalf of the Gemini partnership: the NSF (United States), the Science and Technology Facilities Council (United Kingdom), the National Research Council (Canada), CONICYT (Chile), the Australian Research Council (Australia), the Ministério da Ciência e Tecnologia (Brazil), and SECYT (Argentina).

Facilities: Gemini:Gillett (NIFS/ALTAIR), HST (ACS/WFC)

REFERENCES

Balcells, M., Graham, A. W., & Peletier, R. F. 2007, ApJ, 665, 1084
Becklin, E. E., & Neugebauer, G. 1968, ApJ, 151, 145
Bekki, K. 2007, Publ. Astron. Soc. Australia, 24, 77
Böker, T., Laine, S., van der Marel, R. P., Sarzi, M., Rix, H.-W., Ho, L. C., & Shields, J. C. 2002, AJ, 123, 1389
Böker, T., Sarzi, M., McLaughlin, D. E., van der Marel, R. P., Rix, H.-W., Ho, L. C., & Shields, J. C. 2004, AJ, 127, 105
Cappellari, M., & Copin, Y. 2003, MNRAS, 342, 345
Cappellari, M., & Emsellem, E. 2004, PASP, 116, 138
Carollo, C. M., Stiavelli, M., Seigar, M., de Zeeuw, P. T., & Dejonghe, H. 2002, AJ, 123, 159
Catchpole, R. M., Whitelock, P. A., & Glass, I. S. 1990, MNRAS, 247, 479
Côté, P., et al. 2006, ApJS, 165, 57
Cutri, R. M., et al. 2003, The IRSA 2MASS All-Sky Point Source Catalog (Pasadena: Caltech), http://irsa.ipac.caltech.edu/applications/Gator/nph-dd
Davidge, T. J., Beck, T. L., & McGregor, P. J. 2008, ApJ, 677, 238
de Lorenzi, F., Debattista, V. P., Gerhard, O., & Sambhus, N. 2007, MNRAS, 376, 71
Doyon, R., Joseph, R. D., & Wright, G. S. 1994, ApJ, 421, 101
Ferrarese, L., et al. 2006, ApJ, 644, L21
Garnett, D. R. 2002, ApJ, 581, 1019
Gebhardt, K., et al. 2001, AJ, 122, 2469
Genzel, R., et al. 2003, ApJ, 594, 812
Kleinmann, S. G., & Hall, D. N. B. 1986, ApJS, 62, 501
Kroupa, P. 2001, MNRAS, 322, 231
Lançon, A., Hauschildt, P. H., Ladjal, D., & Mouhcine, M. 2007, A&A, 468, 205
Lauer, T. R., Faber, S. M., Ajhar, E. A., Grillmair, C. J., & Scowen, P. A. 1998, AJ, 116, 2263
Launhardt, R., Zylka, R., & Mezger, P. G. 2002, A&A, 384, 112
Leitherer, C., et al. 1999, ApJS, 123, 3
Lindqvist, M., Habing, H. J., & Winnberg, A. 1992, A&A, 259, 118
Lotz, J. M., Telford, R., Ferguson, H. C., Miller, B. W., Stiavelli, M., & Mack, J. 2001, ApJ, 552, 572
Lu, J. R., Ghez, A. M., Hornstein, S. D., Morris, M., & Becklin, E. E. 2005, ApJ, 625, L51
Maillard, J. P., Paumard, T., Stolovy, S. R., & Rigaut, F. 2004, A&A, 423, 155
Maraston, C. 2005, MNRAS, 362, 799
Marigo, P., Girardi, L., Bressan, A., Groenewegen, M. A. T., Silva, L., & Granato, G. L. 2008, A&A, 482, 883
Mármol-Queraltó, E., Cardiel, N., Cenarro, A. J., Vazdekis, A., Gorgas, J., Pedraz, S., Peletier, R. F., & Sánchez-Blázquez, P. 2008, A&A, in press (arXiv: 0806.0581)
Matthews, L. D., & Wood, K. 2001, ApJ, 548, 150
McGinn, M. T., Sellgren, K., Becklin, E. E., & Hall, D. N. B. 1989, ApJ, 338, 824
McGregor, P. J., et al. 2003, Proc. SPIE, 4841, 1581
Milosavljević, M. 2004, ApJ, 605, L13
Monaco, L., Bellazzini, M., Ferraro, F. R., & Pancino, E. 2005, MNRAS, 356, 1396
Olling, R. P. 1996, AJ, 112, 457
Rossa, J., van der Marel, R. P., Böker, T., Gerssen, J., Ho, L. C., Rix, H.-W., Shields, J. C., & Walcher, C.-J. 2006, AJ, 132, 1074
Schinnerer, E., Böker, T., Emsellem, E., & Lisenfeld, U. 2006, ApJ, 649, 181
Schinnerer, E., Böker, T., & Meier, D. S. 2003, ApJ, 591, L115
Serabyn, E., & Morris, M. 1996, Nature, 382, 602
Seth, A., Agüeros, M., Lee, D., & Basu-Zych, A. 2008, ApJ, 678, 116
Seth, A. C., Dalcanton, J. J., & de Jong, R. S. 2005, AJ, 129, 1331
Seth, A. C., Dalcanton, J. J., Hodge, P. W., & Debattista, V. P. 2006, AJ, 132, 2539
Siegel, M. H., et al. 2007, ApJ, 667, L57
Tremaine, S. D., Ostriker, J. P., & Spitzer, L. 1975, ApJ, 196, 407
van der Marel, R. P., & Franx, M. 1993, ApJ, 407, 525
Walcher, C. J., Böker, T., Charlot, S., Ho, L. C., Rix, H.-W., Rossa, J., Shields, J. C., & van der Marel, R. P. 2006, ApJ, 649, 692
Walcher, C. J., et al. 2005, ApJ, 618, 237
Wehner, E. H., & Harris, W. E. 2006, ApJ, 644, L17
Yoachim, P., & Dalcanton, J. J. 2008, ApJ, 682, 1004